catalysts

MDPI

Article

Noble Metal Single-Atom Coordinated to Nitrogen, Oxygen, and Carbon as Electrocatalysts for Oxygen Evolution

Jianhua Wang [1], Jiangdong Bai [1], Yaqi Cang [1], Qing Li [1], Xing Fan [2,*] and Haiping Lin [1,*]

[1] School of Physics and Information Technology, Shaanxi Normal University, Xi'an 710119, China; liqing@snnu.edu.cn (Q.L.)
[2] Research Center for Carbon-Based Electronics, Key Laboratory for the Physics and Chemistry of Nanodevices, School of Electronics, Peking University, Beijing 100871, China
* Correspondence: xingf@pku.edu.cn (X.F.); hplin@snnu.edu.cn (H.L.)

Abstract: Tuning the coordination environment centering metal atoms has been regarded as a promising strategy to promote the activities of noble metal single-atom catalysts (SACs). In the present work, first-principle calculations are employed to explore the oxygen evolution reaction (OER) performance of Ir and Ru SACs with chemical coordination being nitrogen (M-N_4-C), oxygen (M-O_4-C), and carbon (M-C_4-C) in graphene, respectively. A "three-step" strategy was implemented by progressively investigating these metrics (stability, catalytic activity, structure–activity relationship). A volcano plot of reactivity is established by using the adsorption-free energy of O* (ΔG_{O*}) as a theoretical descriptor. The intrinsic OER activity is IrN_4-C > IrO_4-C > RuO_4-C > RuN_4-C > IrC_4-C > RuC_4-C. The in-depth tuning mechanism of ΔG_{O*} can be indicated and interpreted by the *d*-band centers of the active sites and the crystal orbital Hamilton population analysis of metal-oxygen bonds, respectively.

Keywords: noble metal single-atom catalysts; structure–activity relationship; density functional theory; oxygen evolution reaction; theoretical descriptor

Citation: Wang, J.; Bai, J.; Cang, Y.; Li, Q.; Fan, X.; Lin, H. Noble Metal Single-Atom Coordinated to Nitrogen, Oxygen, and Carbon as Electrocatalysts for Oxygen Evolution. *Catalysts* **2023**, *13*, 1378. https://doi.org/10.3390/catal13101378

Academic Editors: Fengyu Li and Jingxiang Zhao

Received: 25 September 2023
Revised: 16 October 2023
Accepted: 17 October 2023
Published: 19 October 2023

1. Introduction

Electrochemical water splitting is a promising approach for producing highly purified hydrogen using renewable electricity, encompassing both the hydrogen evolution reaction (HER) and the oxygen evolution reaction (OER) [1–5]. Nevertheless, the large-scale application of electrolytic water splitting is hindered by the absence of highly active and cost-effective electrocatalysts to overcome the slow kinetics of the OER. While the prevalent RuO_2 and IrO_2 electrocatalysts are active in driving OER, their large-scale utilization in water-splitting devices is limited by the scarcity [6–8]. As a result, atomically dispersed Ir and Ru atoms fixed on various supporting matrices have attracted extensive attention due to their advantages in minimizing the usage of noble metals and promoting reaction kinetics in OER [9,10]. However, it is noteworthy that carbonaceous supports, renowned for their exceptional conductivity and plentiful defects, provide distinct advantages in supporting single-atom electrocatalysts. These heteroatoms (e.g., N, O, S, P) can be intentionally incorporated and controlled using experimental techniques to achieve the desirable OER performance. Additionally, these heteroatoms can establish stable coordination with the single metal atom, to a certain extent, impeding their aggregation during both the reaction and preparation processes [11]. Interestingly, in this field, the local environments of metal atoms play a crucial role in not only anchoring metal atoms, but also tuning the electronic properties of active sites [12–15]. In recent years, tuning the coordination shell of single-atom catalysts (SACs) using hetero atoms has been widely reported [16–22]. For instance, Wang et al. demonstrated that Co-N_2C_2 exhibited higher selectivity and activity than those of Co-N_3C_1 and Co-N_4 on electroreduction of CO_2 to CO [23]. Zhao et al. revealed that Mo-S_2O_2-C outperformed Mo-N_4-C, Mo-O_4-C, and Mo-S_4-C sites in oxygen reduction reaction (ORR), with a low theoretical onset potential being 0.87 V [19]. Yuan

et al. reported Fe-N_3P as an outstanding ORR catalyst. The limiting potential (1.22 eV) was less than that of Fe-N_4 (1.36 eV) [24]. Jiang et al. revealed that the Ag-N_2C_2 site exhibited much better H_2 evolution activity than the Ag-N_4 site on carbon nitride [25]. Cheng et al. indicated that the hydrogen evolution reaction (HER) activity increases in the order of Mo-O_2N_2, Mo-$O_2N_1C_1$, and Mo-O_2C_2, with overpotentials being 98 mV, 71 mV, and 61 mV at 10 mA cm^{-2} [26]. In addition, SACs have been the subject of extensive research in the field of the OER [27–29]. Niu et al. investigated the OER activity of a single transition metal supported on defective g-C_3N_4 with N vacancy (TM/V_N-CN) using DFT calculations. Their findings revealed that Ru/V_N-CN exhibited exceptional performance with an overpotential being 0.32 V [27]. Wang et al. reported the OER performance of $FeXY_iN_{3-i}$ (X, Y = B, C, O, P, and S; i = 0, 1) moiety in Fe–porphyrin with first-principle calculations, and they indicated that FeC_2N_2-II showed superior catalytic activity with the overpotential being 0.17 V [28]. Su et al. synthesized the Pt_1–C_2N_2 SAC catalyst, which sustained a current density of 120 mA/cm^2 at an overpotential of 405 mV and exhibited a high mass activity of 3350 Ag^{-1} at 232 mV [29]. Given these premises, it is imperative to explore the catalytic performance of Ir and Ru coordinated to N, O, and C as electrocatalysts for OER.

In the present work, OER catalytic activities of three distinct coordination environments of graphene-supported Ir SACs and Ru SACs were comprehensively investigated with density functional theory (DFT) calculations. The catalytic performance of these sites was compared in terms of stability, binding strength of intermediate states, and limiting potentials. A volcano plot of activity was established by using the binding free energy of the oxygen atom (ΔG_{O^*}) as a theoretical descriptor. The ΔG_{O^*} is sensitive to the microenvironments of metal atoms. The in-depth binding characteristics of the key intermediate state O* can be revealed by crystal orbital Hamilton population analysis. The quantitative trend of ΔG_{O^*} of different active sites can be indicated by the *d*-band center of the active sites. This work not only reports IrN_4-C as an outstanding OER catalyst, but also reveals the fundamental structure–activity relationship of single Ir and Ru atoms in different coordination environments.

2. Results and Discussion

2.1. Structures and Stability of Ir, Ru Embedded N_4-C/O_4-C/C_4-C

Figure 1 shows optimized structures of MN_4-C, MO_4-C, and MC_4-C (M = Ir, Ru). In MN_4-C and MO_4-C, all atoms are nearly in the same plane, which is consistent with previous studies [30–32]. In MC_4-C, by contrast, the C atoms in the coordination shell and the M atom protrude out of the graphene substrate. Such structural characteristics can be interpreted by the orbital geometry of sp^2 (O, N) and sp^3 (C) hybridizations. The lattice parameters of MN_4-C, MO_4-C, and MC_4-C (M = Ir, Ru) are a = 12.27 Å~12.30 Å, b = 12.52 Å, and c = 19.82 Å~19.87 Å, which align with a previous study [33]. Experimentally, SACs are often prone to aggregation during synthesis and catalysis, emphasizing the significance of evaluating the thermal stability of SACs in calculations. Currently, comparing the binding energy and cohesive energy of single metal atoms is an effective approach for estimating the thermodynamic stability of SACs [27,34,35]. In this work, the binding energies (E_{bind}) of metal atoms were calculated as shown in Figure 2. The theoretical cohesive energies of bulk Ir and Ru are 5.15 eV and 5.17 eV, respectively [36]. Thus, MN_4-C, MO_4-C, and MC_4-C (M = Ir, Ru) exhibit satisfied stabilities considering that their binding energies are less than −5.00 eV. As seen in Figure 2, the Ir atoms in IrO_4-C and the Ru atoms in RuO_4-C (E_{bind} = −2.19 eV and −2.73 eV, respectively) could potentially undergo aggregation during catalysis. However, the electronic structures and catalytic performance of IrO_4-C and RuO_4-C are still studied in this work in order to obtain the structure–activity relationship.

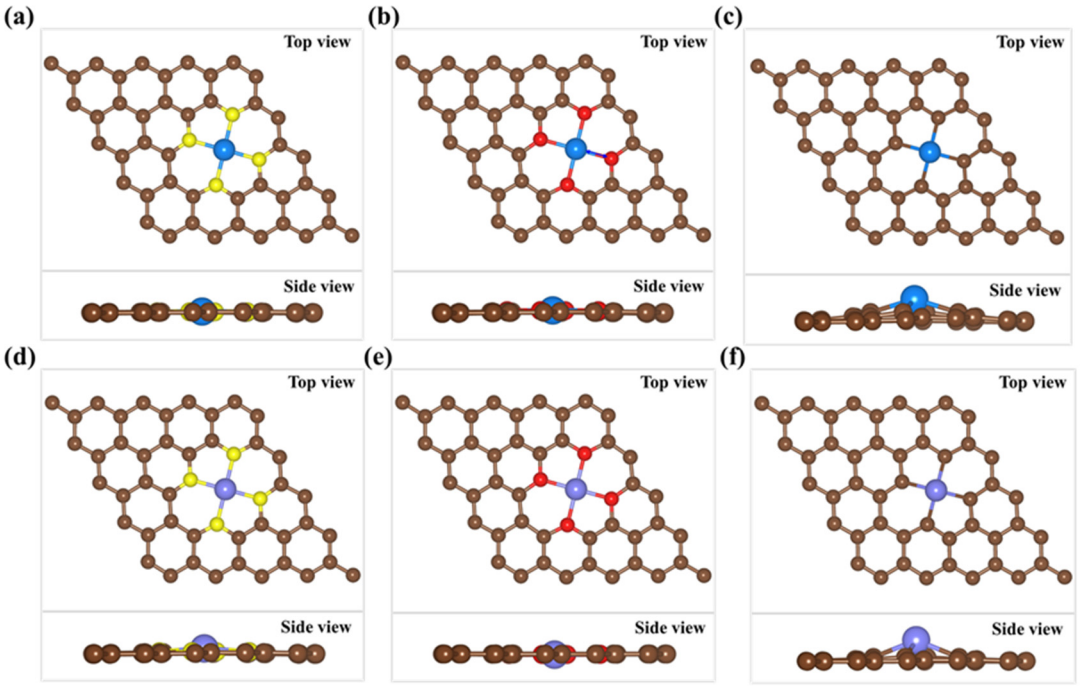

Figure 1. Top and side views of optimized structures of (**a**) IrN_4-C, (**b**) IrO_4-C, (**c**) IrC_4-C, (**d**) RuN_4-C, (**e**) RuO_4-C, and (**f**) RuC_4-C. Ir, Ru, C, N, and O atoms are presented with blue, purple, brown, yellow, and red circles, respectively.

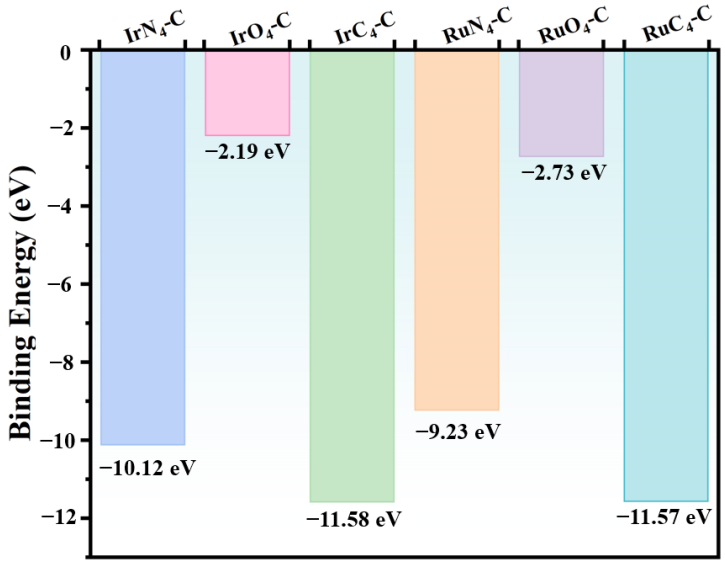

Figure 2. Calculated binding energies of single M atoms in MN_4-C, MO_4-C, and MC_4-C (M = Ir, Ru).

2.2. OER Catalytic Activity

The free energy profiles of OER on MN_4-C, MO_4-C, and MC_4-C (M = Ir, Ru) were explored by DFT calculations. In the traditional adsorbate evolution mechanism (AEM) mechanism, OER involves four proton-coupled electron transfer (PCET) steps, as shown in Scheme 1. The elementary reactions are [37,38]:

$$OH^- + * \rightarrow OH^* + e^-$$

$$OH^* + OH^- \rightarrow O^* + H_2O + e^-$$

$$O^* + OH^- \rightarrow OOH^* + e^-$$

$$OOH^* + OH^- \rightarrow * + O_2\,(g) + H_2O + e^-$$

where * represents the active site of catalysts, and OH*, O*, and OOH* represent three different catalytic intermediates adsorbed on the active site. The first PCET step is the addition of one hydroxyl group to the M (M = Ir, Ru) atom, forming OH* accompanied by the transfer of one electron. Then, OH* further reacts with the second hydroxyl group to attain O*. Subsequently, the third hydroxyl group is absorbed on the surface of O* to give OOH* intermediate. Finally, OOH* combines with the fourth hydroxyl group by PCET, resulting in the release of O_2 and the regeneration of the free active site.

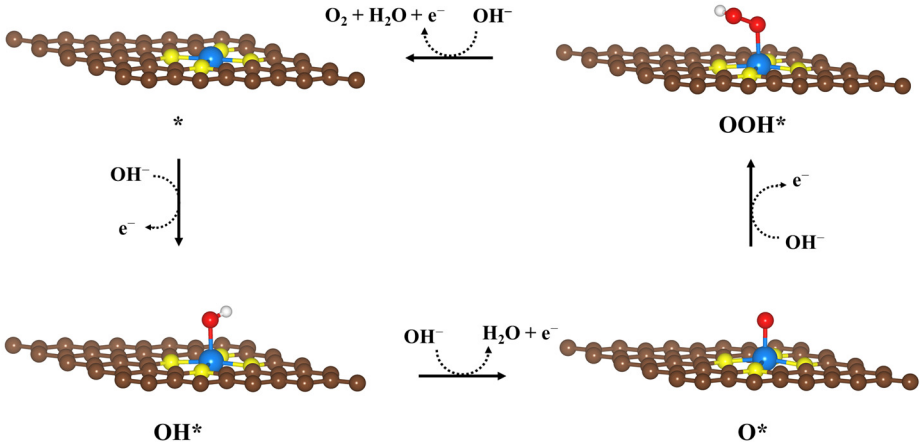

Scheme 1. Schematic of the $4e^-$ process of OER on the MN_4-C, MO_4-C, and MC_4-C (M = Ir, Ru).

The corresponding Gibbs free energy profiles of MN_4-C, MO_4-C, and MC_4-C (M = Ir, Ru) catalysts are shown in Figure 3. Optimized structures of the different catalytic intermediates for OER can be depicted in Figures S1–S6. Gibbs free energy change (ΔG) for each OER reaction step on MN_4-C, MO_4-C, and MC_4-C can be seen in Table S1. In these calculations, the Gibbs free energy of the initial state of OER is defined as 0.00 eV. The cumulative free energy change of the entire OER process is 4.92 eV. By identifying ΔG_{max} [37,39,40], the initial potential and corresponding potential determination step (PDS) can be extracted from the free energy diagrams of the OER processes. As shown in Figure 3a, the second PCET step ($OH^* + OH^- \rightarrow O^* + H_2O + e^-$), which forms the O* intermediate, is the PDS of OER on IrN_4-C. The free energy of all electrochemical reaction steps becomes downhill if the applied potentials are higher than 1.53 eV for IrN_4-C. The η^{OER} value of IrN_4-C is 0.30 V, indicating that IrN_4-C exhibits outstanding catalytic activity towards OER. The PDSs of OER on IrO_4-C, IrC_4-C, RuN_4-C, RuO_4-C, and RuC_4-C are all the third PCET ($O^* + OH^- \rightarrow OOH^* + e^-$) step with the η^{OER} values being 0.51 V, 1.43 V, 0.99 V, 0.62 V, and 1.73 V, respectively (Figure 3b–f). In addition, the first PCET step ($OH^- + * \rightarrow OH^* + e^-$) of OER is exothermic for IrC_4-C, RuN_4-C, and RuC_4-C, whereas other PCETs are endothermic, suggesting that stronger OH* binding leads to poorer activity of IrC_4-C, RuN_4-C, and RuC_4-C. Note that the η^{OER} value of IrN_4-C is at least 0.21 V lower than that of IrO_4-C and IrC_4-C, indicating that the OER catalytic activity of IrN_4-C is significantly better than that of IrO_4-C and IrC_4-C. Similarly, the OER catalytic performance of RuO_4-C is superior to that of RuN_4-C and RuC_4-C (0.62 V vs. 0.99 V and 1.73 V). These reveal that OER activities are closely related to the coordination environment of SACs [41,42]. Moreover, the chemical identity of noble metal atoms also plays a crucial role in tuning the catalytic performance [27]. For instance, the η^{OER} value of IrN_4-C (0.30 V) is smaller than that of RuN_4-C (0.99 V). Thus, the OER activity order of MN_4-C, MO_4-C, and MC_4-C (M = Ir, Ru) is: IrN_4-C > IrO_4-C > RuO_4-C > RuN_4-C > IrC_4-C > RuC_4-C.

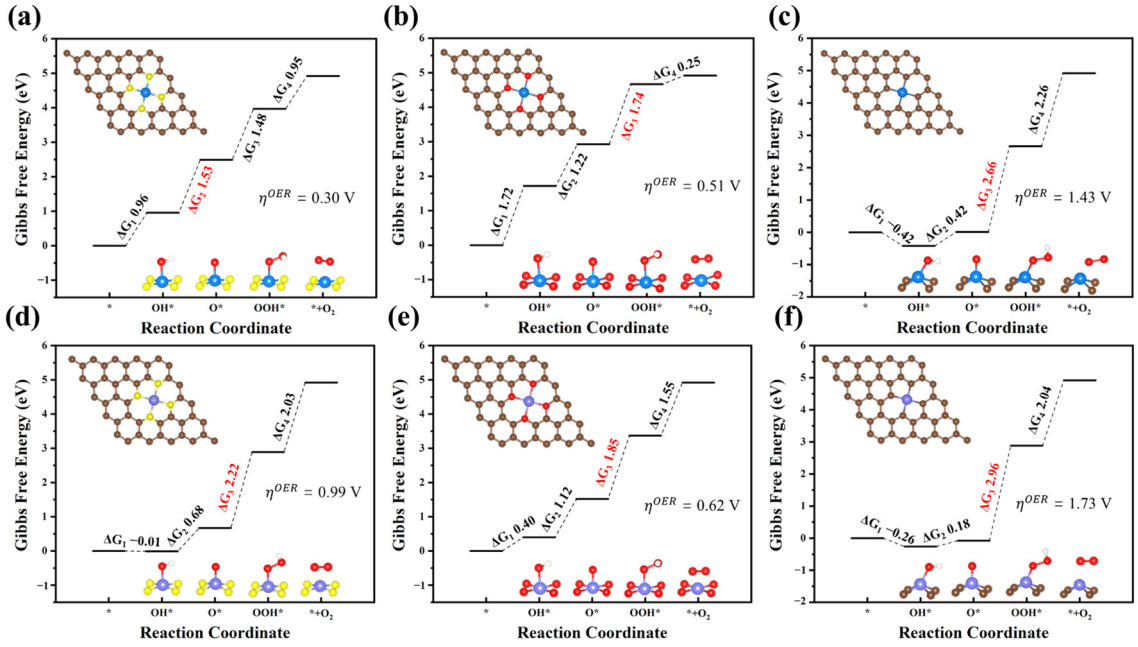

Figure 3. Gibbs free energy diagrams of the OER processes on (**a**) IrN_4-C, (**b**) IrO_4-C, (**c**) IrC_4-C, (**d**) RuN_4-C, (**e**) RuO_4-C, and (**f**) RuC_4-C. H, C, O, N, Ir, and Ru atoms are represented with white, brown, red, yellow, blue, and purple circles.

2.3. Origin of the OER Activity

According to the Sabatier principle [43], too strong or too weak binding interactions of intermediates on catalysts will show a negative impact on energy conversion efficiency. Therefore, the catalytic activities can often be evaluated or predicted by the adsorption energies of intermediates (ΔG_{OH^*}, ΔG_{O^*}, ΔG_{OOH^*}). Table 1 shows that adsorption-free energies of intermediates vary with the metal atoms and their coordination environments. Interestingly, the variation of adsorption-free energies of OOH* and OH* on the catalysts are smaller than 1.38 eV. Nevertheless, the variation of ΔG_{O^*} on different catalysts is much more profound (about 2.48 eV). Thus, the adsorption of O atoms is more sensitive to the microenvironment of active sites than other intermediate states. The OER activity of MN_4-C, MO_4-C, and MC_4-C (M = Ir, Ru) can probably be evaluated by the binding energy of O* (ΔG_{O^*}).

Table 1. The adsorption-free energy of OH*, O*, and OOH* for MN_4-C, MO_4-C, and MC_4-C (M = Ir, Ru).

Systems	IrN_4-C	IrO_4-C	IrC_4-C	RuN_4-C	RuO_4-C	RuC_4-C
ΔG_{OH^*} (eV)	0.96	1.72	−0.42	−0.01	0.40	−0.26
ΔG_{O^*} (eV)	2.49	2.94	0.01	0.67	1.52	−0.08
ΔG_{OOH^*} (eV)	3.97	4.68	2.66	2.89	3.37	2.88

Figure 4a shows that the relationship between ΔG_{OH^*} and ΔG_{OOH^*} can be expressed as $\Delta G_{OOH^*} = 0.95\Delta G_{OH^*} + 3.03$ with a high coefficient of determination ($R^2 = 0.990$). This suggests that ΔG_{OOH^*} rises with increasing ΔG_{OH^*}. Therefore, ΔG_{OOH^*} and ΔG_{OH^*} exhibit almost the same weight when they are used as theoretical descriptors. As shown in Figure S7, however, ΔG_{OOH^*} and ΔG_{OH^*} do not exhibit strong correlations with the catalytic activities. We then plot the *d*-band center with respect to the ΔG_{O^*}. Interestingly, as seen in Figure S8, the linear relationship can only be seen in the planar active sites (M-N_4-C and M-O_4-C). The MC_4-C sites deviated from the scaling relationship due to geometrical distortions. In addition, the formation of O* from OOH* is the PDS of most catalysts. The exception is IrN_4-C, in which the PDS step is the conversion of OH* to

O*. These findings indicate that the η^{OER} can be simultaneously related to the ΔG_{O*}. The volcano plot is therefore established when ΔG_{O*} is selected as a descriptor for OER activity (Figure 4b). It is apparent that IrN_4-C stands on the top of the OER volcano plot with the ΔG_{O*} value being 2.49 eV. IrO_4-C exhibits unsatisfied catalytic efficiency owing to weak O* binding (η^{OER} = 0.51 V). While the IrC_4-C, RuN_4-C, RuO_4-C, and RuC_4-C exhibit small formation energies of O*, also lead to low OER activity (η^{OER} = 1.43 V, 0.99 V, 0.62 V, and 1.73 V, respectively).

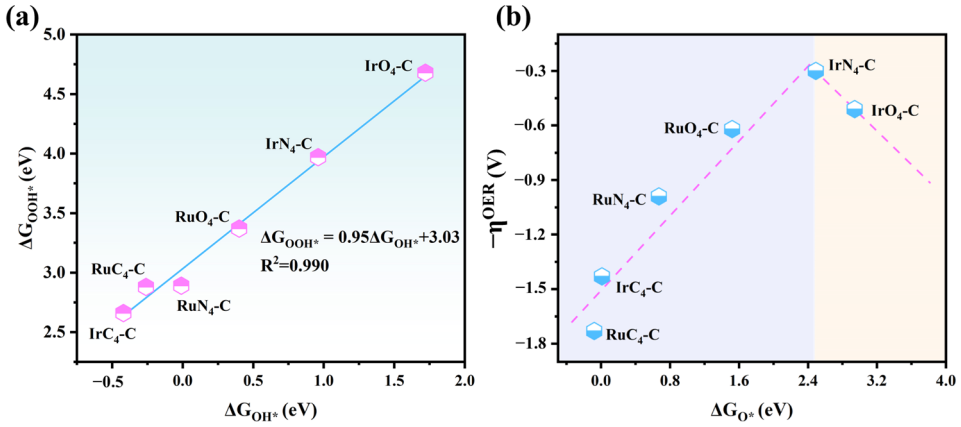

Figure 4. The scaling relationship between (**a**) ΔG_{OOH*} vs. ΔG_{OH*}, and the volcano plot of (**b**) $-\eta^{OER}$ vs. ΔG_{O*} on MN_4-C, MO_4-C, and MC_4-C (M = Ir, Ru).

Subsequently, crystal orbital Hamilton populations (COHP) and integrated COHP (ICOHP) are employed to describe the adsorption trend of intermediated states [44–46]. COHP is a prevalent method to analyze the bonding characteristics between atoms in chemical species and can often provide important information in the study of structure–activity relationships. For instance, Yan et al. demonstrated that there is a strong linear relationship between the ΔG_{OH*} and ICOHP with an R^2 of 0.91, explaining the OH* adsorption trend. Thus, the Co-N-C/GDY achieved superior OER performance due to its moderate binding strength with OH* species [45]. Wang et al. revealed that the bonding strength between the 3*d* metal atom and O* intermediate generally decreases with the atomic number increases for different MBene substrates by employing ICOHP calculations [46]. The binding strength of the M-O bond in MN_4-C-O*, MO_4-C-O*, and MC_4-C-O* (M = Ir, Ru) can be further examined by COHP analysis. As depicted in Figure 5, the bonding (–COHP > 0) and antibonding (–COHP < 0) contributions in each M-O bond are shown on the right and left panels, respectively. The ICOHP values of the M-O bond in IrO_4-C-O* (−4.14 eV) are more than that in IrN_4-C-O* (−5.24 eV). The ICOHP values of the M-O bond in IrC_4-C-O*, RuN_4-C-O*, RuO_4-C-O*, and RuC_4-C-O* are −6.88 eV, −6.62 eV, −5.57 eV, and −8.45 eV, respectively, which is more negative compared to IrN_4-C-O*. These findings reveal that the binding strength of the oxygen atom in IrO_4-C is weaker than that in IrN_4-C, while the strong binding of the oxygen atom is observed in IrC_4-C, RuN_4-C, RuO_4-C, and RuC_4-C compared to IrN_4-C. Thus, IrN_4-C exhibits excellent catalytic OER performance in these catalysts due to the moderate adsorption energy of O*. The OER performance of MN_4-C, MO_4-C, and MC_4-C (M = Ir, Ru) could be evaluated by the binding energy of O* (ΔG_{O*}), which is consistent with the above discussions about the volcano plot in Figure 4b.

As it has been demonstrated that ΔG_{O*} is a theoretical descriptor to evaluate the OER activity, it is important to study the structure–property relationship between the binding energy of O* and the microstructure of the active sites. The charge density difference (CDD) of MN_4-C, MO_4-C, and MC_4-C (M = Ir, Ru) was examined with iso-surfaces set at 0.015 e/Å^3. As shown in Figure 6, electrons transfer (0.54 e~0.82 e) from M atoms to the N_4-C/O_4-C/C_4-C substrate (Tables S3 and S4). Such charge redistributions are consistent with CDD analysis, showing the accumulation of significant positive charges (pink area) around the anchored M atoms (Figure 6). It is worth noting that formal charges carried by metal

atoms are strongly dependent on coordination shells. For instance, the Bader charge of Ir atoms are +0.56 |e| and +0.72 |e| on the C_4-C and N_4-C substrates, respectively. Notably, the *d*-band center (ε_d) has been extensively employed as an effective descriptor to establish the relation between the intrinsic electronic properties of catalysts and their adsorption behaviors [27,47]. For instance, Niu et al. established a linear correlation between the ε_d and the adsorption energy of OER intermediates, providing a quantitative description of adsorption energies and revealing the origin of activity based on electronic structures. Consequently, Ru embedded in defective g-C_3N_4 exhibits exceptional performance, with an overpotential as low as 0.32 V [27]. Yang et al. demonstrated that the overpotential of CoNi in nitrogen-doped graphene shows a volcano-shaped relationship with the ε_d of the catalytic site Co. This suggests that the ε_d of the catalytic site is a critical parameter influencing the OER activity [47]. The partial density of states (PDOS) of *d* orbitals for M atoms on MN_4-C, MO_4-C, and MC_4-C (M = Ir, Ru) are shown in Figure 7. As can be seen, replacing carbon with oxygen or nitrogen for coordination with M metal shifts the ε_d of the M atom toward the Fermi level (E_f). For example, the ε_d values for Ir atoms on IrN_4-C, IrO_4-C, and IrC_4-C exhibit the following trend: IrN_4-C (−1.86 eV) > IrO_4-C (−2.20 eV) > IrC_4-C (−2.60 eV). In addition, the ε_d values for Ru atoms on the C_4-C, O_4-C, and N_4-C substrates are −1.81 eV, −1.10 eV, and −1.07 eV (Figure 7b), respectively. The closer the ε_d of the active site is to the Fermi level, the stronger its ability to participate in capturing reaction intermediates and forming bonds, resulting in higher catalytic activity. Specifically speaking, a more negative ε_d is related to weaker adsorption [48,49]. However, in Ru SACs, the activity of RuO_4-C surpasses that of RuC_4-C and Ru-N_4-C. It is explicable that the association between the ε_d and catalytic performance is merely a qualitative description and not a quantitative trend. Thus, the moderate ε_d value of Ir atoms on IrN_4-C can lead to a neither too strong nor too weak binding strength of oxygen atom (ΔG_{O^*}). As a result, IrN_4-C shows excellent OER performance with the lower overpotential being 0.30 V.

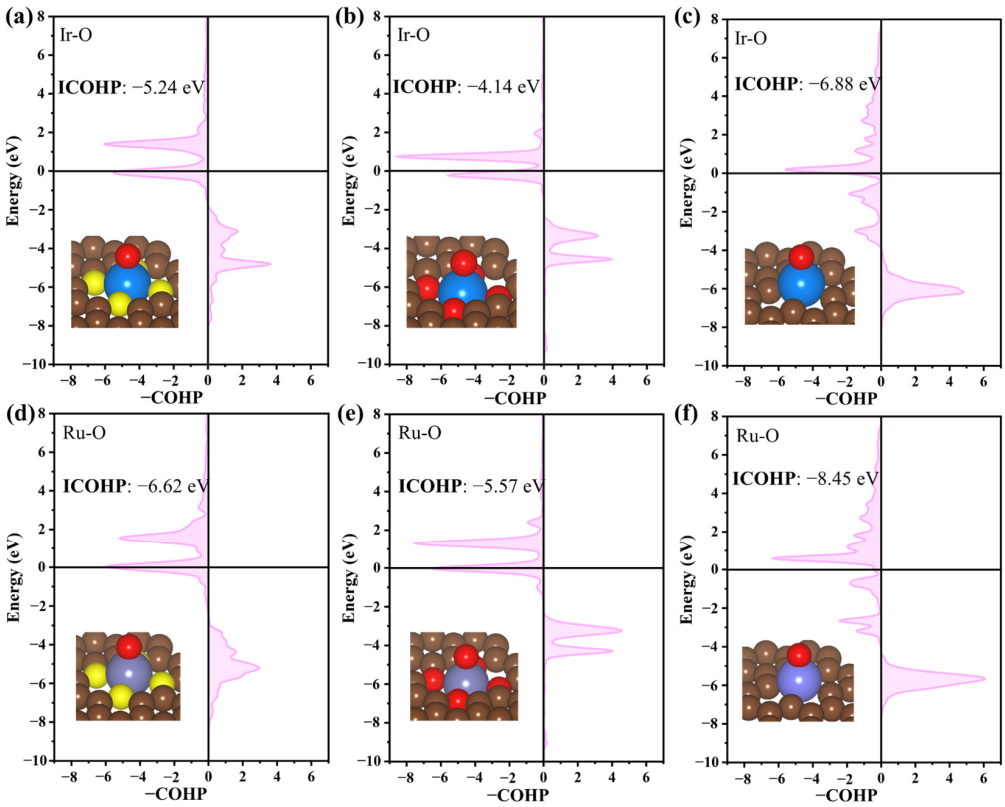

Figure 5. Projected crystal orbital Hamilton populations (COHP) between chemisorbed O* and active metal centers on (**a**) IrN_4-C, (**b**) IrO_4-C, (**c**) IrC_4-C, (**d**) RuN_4-C, (**e**) RuO_4-C, and (**f**) RuC_4-C. The Fermi levels were set to the energy zero.

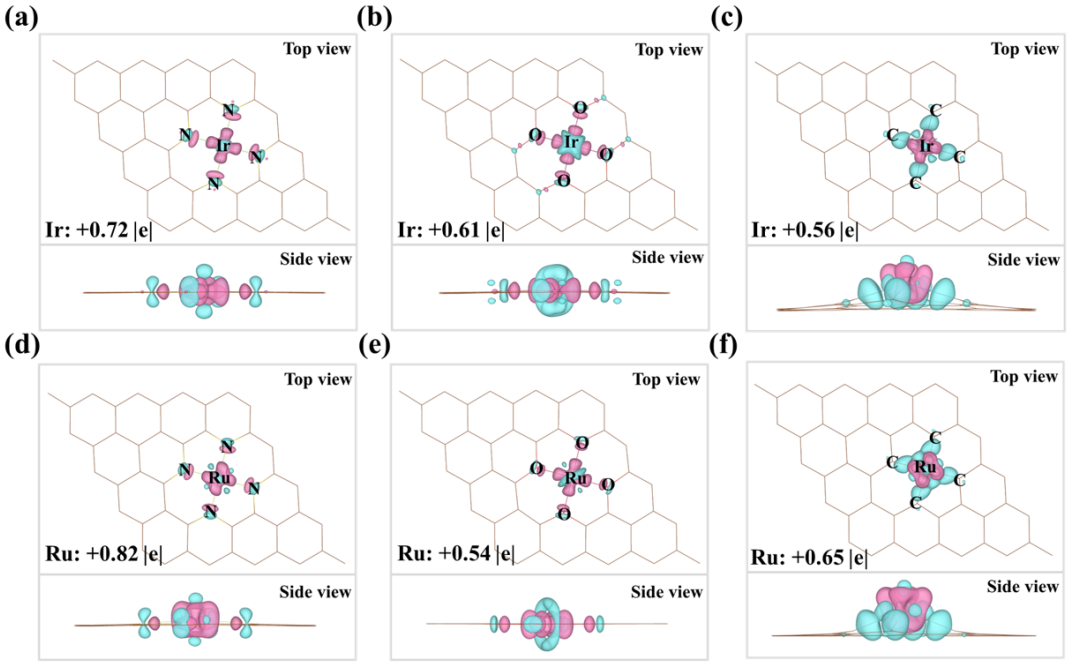

Figure 6. The CDD of (**a**) IrN_4-C, (**b**) IrO_4-C, (**c**) IrC_4-C, (**d**) RuN_4-C, (**e**) RuO_4-C, and (**f**) RuC_4-C. The electron accumulation and depletion are represented with cyan and pink contours, with iso-surfaces being 0.015 e/Å^3. The net charge of M atoms of MN_4-C, MO_4-C, and MC_4-C (M = Ir, Ru).

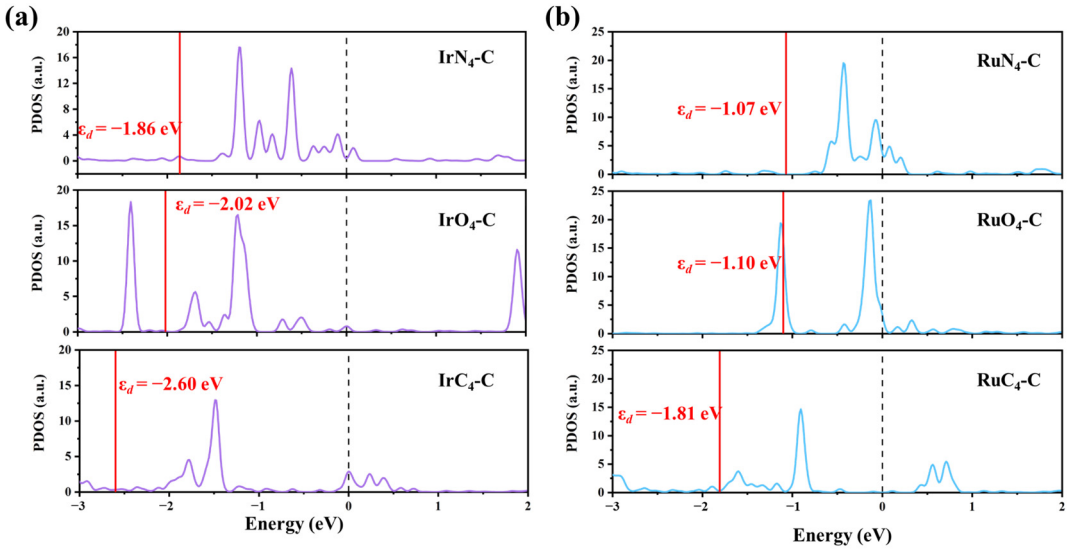

Figure 7. Partial density of states (PDOS) of *d* orbitals for M atoms on (**a**) IrN_4-C, IrO_4-C and IrC_4-C, (**b**) RuN_4-C, RuO_4-C and RuC_4-C. The *d*-band centers (ε_d) are also labeled for metal atoms. The Fermi level (E_f) is set to 0.00 eV.

2.4. Solvent Effects

Given that OER takes place in aqueous electrolytes, the impact of solvent effects in the reaction pathways of MN_4-C, MO_4-C, and MC_4-C (M = Ir, Ru) has also been investigated using an implicit solvent model. The Gibbs free energy profiles of OER on MN_4-C, MO_4-C, and MC_4-C (M = Ir, Ru) catalysts in a vacuum (black lines) and implicit solvent model (red lines) are shown in Figure S9. Gibbs free energy changes (ΔG) for each OER reaction step on MN_4-C, MO_4-C, and MC_4-C can be seen in Table S5. The third PCET ($O^* + OH^- \rightarrow OOH^* + e^-$) is the PDS of OER on MN_4-C, MO_4-C, and MC_4-C (M = Ir, Ru) in the implicit

solvent model, which is quite consistent with those in the vacuum. As can be seen in Figure S8, the η^{OER} value of IrN_4-C is 0.33 V in the implicit solvent model, which is only slightly increased by 0.03 V (η^{OER} = 0.30 V in a vacuum). The η^{OER} values of IrO_4-C and RuO_4-C are 0.71 V and 0.67 V in the implicit solvent model, which are 0.20 V and 0.05 V higher than that in a vacuum, respectively. The η^{OER} values of IrC_4-C and RuC_4-C are 1.34 V and 1.58 V in the implicit solvent model, which is 0.09 V and 0.15 V less than that in a vacuum. These results are from the diverse influence of the implicit solvent model on ΔG_{O^*}. In addition, the adsorption-free energy of *OH on IrC_4-C, RuN_4-C, and RuC_4-C is decreased compared with that in a vacuum, indicating stronger interactions between the O atom and the M (M = Ir, Ru) atom. While the overpotential of MN_4-C, MO_4-C, and MC_4-C (M = Ir, Ru) increases by -0.15 V~0.20 V, the qualitative trends of the influence of coordination shells are not affected by the solvation. This finding aligns well with recent research reports [50–52]. Zhang et al. reported that in the implicit solvent model, the onset potential of Pt (111) increases by 0.11 V compared to that in a vacuum, and the ORR performance trend of metal surfaces is consistent with that in a vacuum [51]. Peng et al. showed that including solvent effects increases the overpotential of the Fe- or Ni-doped Co_3O_4(001) by around 0.20 V~0.40 V. However, the general OER activity trends of Fe- or Ni-doped Co_3O_4(001) remain unchanged [52]. Therefore, our results demonstrate that the implicit solvent model can enhance O* adsorption by finely tuning the OER activity. Additionally, the implicit solvent model has a minor impact on the Gibbs free energy profile. The trend of catalytic performance in the implicit solvent model closely mirrors that observed in vacuum. IrN_4-C exhibits excellent OER catalytic performance compared to IrO_4-C, IrC_4-C, RuN_4-C, RuO_4-C, and RuC_4-C.

2.5. Structural Distortions and OER Activity

The impact of structural distortions at the evaluated coordination sites on catalytic activity was thoroughly investigated. Among the various SACs studied, IrC_4-C and Ru-C_4-C exhibit the most pronounced structural distortions. Notably, these structural deformations lead to a situation where the single metal atom protrudes from the C_4-C substrate, resulting in excessively strong binding with O* intermediates. Consequently, IrC_4-C and Ru-C_4-C show poor catalytic performance in OER. In addition, RuN_4-C displays minor structural distortions in comparison to IrN_4-C, IrO_4-C, and RuO_4-C, which shows small formation energies of O*, and also leads to low OER activity. These findings indicated that structural distortions induce a strong interaction between the metal atom and reaction intermediates, consequently impeding the efficiency of the oxygen evolution reaction. This discovery provides invaluable insights for the ongoing efforts to optimize catalyst design and achieve enhanced catalytic performance.

3. Computational Methods

All DFT calculations were carried out using a plane-wave basis set within the Vienna Ab Initio Simulation Package (VASP 5.4.4) [53–55]. The exchange–correlation function was described by the Perdew–Burke–Ernzerhof (PBE) parameterization of the generalized gradient approximation (GGA) [56–59]. The projector-augmented wave (PAW) approximation was adopted to describe the ion–electron interactions [60]. The plane-waves expansion of the Kohn–Sham orbitals was expanded to a kinetic energy cutoff of 400 eV. Then, 10^{-4} eV was set as the convergence criteria for the energy, and -0.02 eV/Å was set as the convergence criteria for the forces on each atom. The DFT-D3 method with Becke–Jonson damping was adopted to accurately describe the long-range van der Waals (vdW) interactions [61]. The solvation effect was evaluated under an implicit solvent model VASPsol [62].

MN_4-C, MO_4-C, and MC_4-C (M = Ir, Ru) catalysts were constructed by embedding an M atom in N_4-C, O_4-C, and C_4-C cavities, respectively. A vacuum thickness of more than 15 Å in the vertical direction was utilized to avoid interactions between periodic images. The Brillouin zone was sampled using a $2 \times 2 \times 1$ gamma-centered k-point mesh for structural optimizations, while a denser k-point mesh of $4 \times 4 \times 1$ was employed

for electronic property computations. The binding energy (E_{bind}) was calculated using the equation:

$$E_{bind} = E_{total} - E_{substrate} - E_M \quad (1)$$

where E_{total}, $E_{substrate}$, and E_M are energies of the catalysts, doped graphene substrates, and an isolated M atom in a vacuum, respectively. The adsorption energy of three different catalytic intermediates can be described as follows:

$$\Delta E_{OH^*} = E_{OH^*} + 1/2E_{H_2} - E_* - E_{H_2O} \quad (2)$$

$$\Delta E_{O^*} = E_{O*} + E_{H_2} - E_* - E_{H_2O} \quad (3)$$

$$\Delta E_{OOH^*} = E_{OOH^*} + 3/2E_{H_2} - E_* - 2E_{H_2O} \quad (4)$$

where E_*, E_{OH^*}, E_{O^*}, and E_{OOH^*} are energies of the clean catalyst substrate, and surfaces adsorbed by OH*, O*, and OOH* species, respectively. E_{H_2O} and E_{H_2} are energies of H_2O and H_2 molecules in gas phases, as shown in Table S6. The adsorption-free energies can be obtained in the equation:

$$\Delta G_{ads} = \Delta E_{ads} + \Delta E_{ZPE} - T\Delta S \quad (5)$$

where E_{ads} and E_{ZPE} are the adsorption energy and zero-point energy, respectively. T is fixed at 298.15 K in this study and S is the entropy. For all OER steps on MN_4-C, MO_4-C, and MC_4-C (M = Ir, Ru) catalysts, the Gibbs free energy change (ΔG) can be calculated by the following expression [63]:

$$\Delta G = \Delta E + \Delta E_{ZPE} - T\Delta S + \Delta G_{pH} \quad (6)$$

where E is the energy of the reactant and product obtained from DFT computations directly. $\Delta G_{pH} = k_B T \ln 10 \times pH$ represents the free energy contribution due to the variations in the H concentration, where k_B is the Boltzmann constant. In this work, the pH value was set to 14. The theoretical OER overpotential (η^{OER}) for a given electrocatalyst can be defined as [64]:

$$\eta^{OER} = \max\{\Delta G_1, \Delta G_2, \Delta G_3, \Delta G_4\}/e - 1.23\ V \quad (7)$$

where ΔG_i (i = 1, 2, 3, 4) represents the Gibbs free energy change for each step of OER, and the value of 1.23 eV is the equilibrium overpotential of OER. The charge density difference was obtained by the following equation:

$$\Delta\rho = \rho_{AB} - \rho_A - \rho_B \quad (8)$$

where ρ_{AB}, ρ_A, and ρ_B are electron densities of complexes, substrates, and adsorbates, respectively.

4. Conclusions

In summary, by means of first-principle calculations, the theoretical increase in OER activity on MN_4-C, MO_4-C, and MC_4-C (M = Ir, Ru) was IrN_4-C > IrO_4-C > RuO_4-C > RuN_4-C > IrC_4-C > RuC_4-C in the alkaline media. In particular, IrN_4-C exhibits outstanding OER performance with a low overpotential of 0.30 V. Our calculations indicate that the weak binding of O* to IrO_4-C results in poor catalyst activity, and the strong binding of O* is responsible for the lower OER activity observed in IrC_4-C, RuN_4-C, RuO_4-C, and RuC_4-C. Furthermore, the analysis of COHP and PDOS highlights the enhancement of electrocatalytic activity with the tuning of the coordination shells of M atoms, which effectively adjusts the electronic structure of M atoms to balance the binding strength of O*. Our study challenges traditional thinking and inspires more theoretical and experimental investigations into exploring the catalytic properties of SACs by considering different coordination environments with other metals.

Supplementary Materials: The following supporting information can be downloaded at: https://www.mdpi.com/article/10.3390/catal13101378/s1, Figure S1: Optimized structures of (**a**) IrN_4-C catalyst and (**b**–**d**) OER intermediates along the pathway on IrN_4-C. Ir, C, N, H, and O atoms are presented with blue, brown, yellow, white, and red circles, respectively. Figure S2: Optimized structure of (**a**) IrO_4-C catalyst and (**b**–**d**) OER intermediates along the pathway on IrO_4-C. Ir, C, H, and O atoms are presented with blue, brown, white, and red circles, respectively. Figure S3: Optimized structure of (**a**) IrC_4-C catalyst and (**b**–**d**) OER intermediates along the pathway on IrC_4-C. Ir, C, H, and O atoms are presented with blue, brown, white, and red circles, respectively. Figure S4: Optimized structure of (**a**) RuN_4-C catalyst and (**b**–**d**) OER intermediates along the pathway on RuN_4-C. Ru, C, N, H, and O atoms are presented with purple, brown, yellow, white, and red circles, respectively. Figure S5: Optimized structure of (**a**) RuO_4-C catalyst and (**b**–**d**) OER intermediates along the pathway on RuO_4-C. Ru, C, H, and O atoms are presented with purple, brown, white, and red circles, respectively. Figure S6: Optimized structure of (**a**) RuC_4-C catalyst and (**b**–**d**) OER intermediates along the pathway on RuC_4-C. Ru, C, H, and O atoms are presented with purple, brown, white, and red circles, respectively. Figure S7: The scaling relationship between (**a**) ΔG_{OH^*} vs. η^{OER}, (**b**) ΔG_{OOH^*} vs. η^{OER} on MN_4-C, MO_4-C, and MC_4-C (M = Ir, Ru). Figure S8: The scaling relationship between ΔG_{O^*} vs. *d*-band center on MN_4-C, MO_4-C, and MC_4-C (M = Ir, Ru). Figure S9: Free energy diagrams of OER processes on (**a**) IrN_4-C, (**b**) IrO_4-C, (**c**) IrC_4-C, (**d**) RuN_4-C, (**e**) RuO_4-C, and (**f**) RuC_4-C in vacuum (black lines) and implicit solvent model (red lines), respectively. H, C, O, N, Ir, and Ru atoms are represented with white, brown, red, yellow, blue, and purple circles. Table S1: Gibbs free energy change (ΔG) for each OER reaction step on MN_4-C, MO_4-C, and MC_4-C (M = Ir, Ru) in vacuum. Table S2: The *d*-band center of M atom on MN_4-C, MO_4-C, and MC_4-C (M = Ir, Ru). Table S3: Bader charges of IrN_4, IrO_4-C, IrC_4-C. The ZVAL represents the number of valent electrons in each atomic sphere. Table S4: Bader charges of RuN_4, RuO_4-C, and RuC_4-C. The ZVAL represents the number of valent electrons in each atomic sphere. Table S5: Gibbs free energy change (ΔG) for each OER reaction step on MN_4-C, MO_4-C, and MC_4-C (M = Ir, Ru) with an implicit solvent model. Table S6: The calculated total energies (E) and thermodynamic quantities for the gas phase H_2 species (T = 298.15 K, P = 1 bar), and free H_2O at 298.15 K, 0.035 bar.

Author Contributions: Conceptualization, J.B.; methodology, Y.C.; investigation, J.W., J.B. and Y.C.; data curation, J.W., J.B., Y.C., Q.L., X.F. and H.L.; writing—original draft preparation, J.W.; writing—review and editing, H.L. and X.F.; supervision, Q.L., X.F. and H.L. All authors have read and agreed to the published version of the manuscript.

Funding: This research was funded by the National Natural Science Foundation of China (Grants 22373063, 22302005, 22272099, and 22072102), Fundamental Research Funds for the Central Universities of China (Grants GK202203002, GK202201001, and GK202301001), and China Postdoctoral Science Foundation (2023M730044).

Data Availability Statement: The data presented in this study are available on request from the corresponding authors.

Acknowledgments: We gratefully acknowledge Shaanxi Normal University's high-performance computing infrastructure SNNUGrid (HPC Centers: QiLin AI LAB) for providing computer facilities.

Conflicts of Interest: The authors declare no conflict of interest.

References

1. Luyen Doan, T.L.; Tran, D.T.; Nguyen, D.C.; Tuan Le, H.; Kim, N.H.; Lee, J.H. Hierarchical three-dimensional framework interface assembled from oxygen-doped cobalt phosphide layer-shelled metal nanowires for efficient electrocatalytic water splitting. *Appl. Catal. B* **2020**, *261*, 118268. [CrossRef]
2. Shi, Y.; Zhang, B. Recent advances in transition metal phosphide nanomaterials: Synthesis and applications in hydrogen evolution reaction. *Chem. Soc. Rev.* **2016**, *45*, 1529–1541. [CrossRef]
3. Zheng, Y.; Jiao, Y.; Jaroniec, M.; Qiao, S.Z. Advancing the Electrochemistry of the Hydrogen-Evolution Reaction through Combining Experiment and Theory. *Angew. Chem. Int. Ed.* **2015**, *54*, 52–65. [CrossRef]
4. Xu, X.; Su, C.; Shao, Z. Fundamental Understanding and Application of $Ba_{0.5}Sr_{0.5}Co_{0.8}Fe_{0.2}O_{3-\delta}$ Perovskite in Energy Storage and Conversion: Past, Present, and Future. *Energy Fuels* **2021**, *35*, 13585–13609. [CrossRef]
5. Tang, J.; Xu, X.; Tang, T.; Zhong, Y.; Shao, Z. Perovskite-Based Electrocatalysts for Cost-Effective Ultrahigh-Current-Density Water Splitting in Anion Exchange Membrane Electrolyzer Cell. *Small Methods* **2022**, *6*, 2201099. [CrossRef]

6. Jin, H.; Guo, C.; Liu, X.; Liu, J.; Vasileff, A.; Jiao, Y.; Zheng, Y.; Qiao, S.-Z. Emerging Two-Dimensional Nanomaterials for Electrocatalysis. *Chem. Rev.* **2018**, *118*, 6337–6408. [CrossRef]
7. Liu, J.; Zhang, T.; Waterhouse, G.I.N. Complex alloy nanostructures as advanced catalysts for oxygen electrocatalysis: From materials design to applications. *J. Mater. Chem. A* **2020**, *8*, 23142–23161. [CrossRef]
8. Liu, J.; Zhu, D.; Guo, C.; Vasileff, A.; Qiao, S.-Z. Design Strategies toward Advanced MOF-Derived Electrocatalysts for Energy-Conversion Reactions. *Adv. Energy Mater.* **2017**, *7*, 1700518. [CrossRef]
9. Wang, A.; Li, J.; Zhang, T. Heterogeneous single-atom catalysis. *Nat. Rev. Chem.* **2018**, *2*, 65–81. [CrossRef]
10. Chen, Y.; Ji, S.; Chen, C.; Peng, Q.; Wang, D.; Li, Y. Single-Atom Catalysts: Synthetic Strategies and Electrochemical Applications. *Joule* **2018**, *2*, 1242–1264. [CrossRef]
11. Chen, Y.-N.; Zhang, X.; Zhou, Z. Carbon-Based Substrates for Highly Dispersed Nanoparticle and Even Single-Atom Electrocatalysts. *Small Methods* **2019**, *3*, 1900050. [CrossRef]
12. Wu, J.; Zhou, H.; Li, Q.; Chen, M.; Wan, J.; Zhang, N.; Xiong, L.; Li, S.; Xia, B.Y.; Feng, G.; et al. Densely Populated Isolated Single Co–N Site for Efficient Oxygen Electrocatalysis. *Adv. Energy Mater.* **2019**, *9*, 1900149. [CrossRef]
13. Wu, J.; Xiong, L.; Zhao, B.; Liu, M.; Huang, L. Densely Populated Single Atom Catalysts. *Small Methods* **2020**, *4*, 1900540. [CrossRef]
14. Chen, S.; Luo, T.; Li, X.; Chen, K.; Fu, J.; Liu, K.; Cai, C.; Wang, Q.; Li, H.; Chen, Y.; et al. Identification of the Highly Active Co–N_4 Coordination Motif for Selective Oxygen Reduction to Hydrogen Peroxide. *J. Am. Chem. Soc.* **2022**, *144*, 14505–14516. [CrossRef] [PubMed]
15. Huang, J.; Zhang, Q.; Ding, J.; Zhai, Y. Fe–N–C single atom catalysts for the electrochemical conversion of carbon, nitrogen and oxygen elements. *Mater. Rep. Energy* **2022**, *2*, 100141. [CrossRef]
16. Li, Y.; Wu, Z.-S.; Lu, P.; Wang, X.; Liu, W.; Liu, Z.; Ma, J.; Ren, W.; Jiang, Z.; Bao, X. High-Valence Nickel Single-Atom Catalysts Coordinated to Oxygen Sites for Extraordinarily Activating Oxygen Evolution Reaction. *Adv. Sci.* **2020**, *7*, 1903089. [CrossRef]
17. Zhao, Y.; Guo, Y.; Lu, X.F.; Luan, D.; Gu, X.; Lou, X.W. Exposing Single Ni Atoms in Hollow S/N-Doped Carbon Macroporous Fibers for Highly Efficient Electrochemical Oxygen Evolution. *Adv. Mater.* **2022**, *34*, 2203442. [CrossRef]
18. Fan, L.; Liu, P.F.; Yan, X.; Gu, L.; Yang, Z.Z.; Yang, H.G.; Qiu, S.; Yao, X. Atomically isolated nickel species anchored on graphitized carbon for efficient hydrogen evolution electrocatalysis. *Nat. Commun.* **2016**, *7*, 10667. [CrossRef]
19. Zhao, Y.; Zhang, Z.; Liu, L.; Wang, Y.; Wu, T.; Qin, W.; Liu, S.; Jia, B.; Wu, H.; Zhang, D.; et al. S and O Co-Coordinated Mo Single Sites in Hierarchically Porous Tubes from Sulfur–Enamine Copolymerization for Oxygen Reduction and Evolution. *J. Am. Chem. Soc.* **2022**, *144*, 20571–20581. [CrossRef]
20. Ling, C.; Ouyang, Y.; Li, Q.; Bai, X.; Mao, X.; Du, A.; Wang, J. A General Two-Step Strategy–Based High-Throughput Screening of Single Atom Catalysts for Nitrogen Fixation. *Small Methods* **2019**, *3*, 1800376. [CrossRef]
21. Zang, W.; Sun, T.; Yang, T.; Xi, S.; Waqar, M.; Kou, Z.; Lyu, Z.; Feng, Y.P.; Wang, J.; Pennycook, S.J. Efficient Hydrogen Evolution of Oxidized Ni-N_3 Defective Sites for Alkaline Freshwater and Seawater Electrolysis. *Adv. Mater.* **2021**, *33*, 2003846. [CrossRef] [PubMed]
22. Zang, W.; Yang, T.; Zou, H.; Xi, S.; Zhang, H.; Liu, X.; Kou, Z.; Du, Y.; Feng, Y.P.; Shen, L.; et al. Copper Single Atoms Anchored in Porous Nitrogen-Doped Carbon as Efficient pH-Universal Catalysts for the Nitrogen Reduction Reaction. *ACS Catal.* **2019**, *9*, 10166–10173. [CrossRef]
23. Wang, X.; Chen, Z.; Zhao, X.; Yao, T.; Chen, W.; You, R.; Zhao, C.; Wu, G.; Wang, J.; Huang, W.; et al. Regulation of Coordination Number over Single Co Sites: Triggering the Efficient Electroreduction of CO_2. *Angew. Chem. Int. Ed.* **2018**, *57*, 1944–1948. [CrossRef] [PubMed]
24. Yuan, K.; Lützenkirchen-Hecht, D.; Li, L.; Shuai, L.; Li, Y.; Cao, R.; Qiu, M.; Zhuang, X.; Leung, M.K.H.; Chen, Y.; et al. Boosting Oxygen Reduction of Single Iron Active Sites via Geometric and Electronic Engineering: Nitrogen and Phosphorus Dual Coordination. *J. Am. Chem. Soc.* **2020**, *142*, 2404–2412. [CrossRef] [PubMed]
25. Jiang, X.-H.; Zhang, L.-S.; Liu, H.-Y.; Wu, D.-S.; Wu, F.-Y.; Tian, L.; Liu, L.-L.; Zou, J.-P.; Luo, S.-L.; Chen, B.-B. Silver Single Atom in Carbon Nitride Catalyst for Highly Efficient Photocatalytic Hydrogen Evolution. *Angew. Chem. Int. Ed.* **2020**, *59*, 23112–23116. [CrossRef] [PubMed]
26. Cheng, C.C.; Yeh, Y.X.; Ting, Y.C.; Lin, S.H.; Sasaki, K.; Choi, Y.; Lu, S.Y. Modulation of the coordination environment enhances the electrocatalytic efficiency of Mo single atoms toward water splitting. *J. Mater. Chem. A* **2022**, *10*, 8784–8797. [CrossRef]
27. Niu, H.; Wan, X.; Wang, X.; Shao, C.; Robertson, J.; Zhang, Z.; Guo, Y. Single-Atom Rhodium on Defective g-C_3N_4: A Promising Bifunctional Oxygen Electrocatalyst. *ACS Sustain. Chem. Eng.* **2021**, *9*, 3590–3599. [CrossRef]
28. Wang, S.; Huang, B.; Dai, Y.; Wei, W. Tuning the Coordination Microenvironment of Central Fe Active Site to Boost Water Electrolysis and Oxygen Reduction Activity. *Small* **2023**, *19*, 2205111. [CrossRef]
29. Su, H.; Soldatov, M.A.; Roldugin, V.; Liu, Q. Platinum single-atom catalyst with self-adjustable valence state for large-current-density acidic water oxidation. *eScience* **2022**, *2*, 102–109. [CrossRef]
30. Xue, Z.; Zhang, X.; Qin, J.; Liu, R. TMN_4 complex embedded graphene as bifunctional electrocatalysts for high efficiency OER/ORR. *J. Energy Chem.* **2021**, *55*, 437–443. [CrossRef]
31. Xiao, M.; Zhu, J.; Li, G.; Li, N.; Li, S.; Cano, Z.P.; Ma, L.; Cui, P.; Xu, P.; Jiang, G.; et al. A Single-Atom Iridium Heterogeneous Catalyst in Oxygen Reduction Reaction. *Angew. Chem. Int. Ed.* **2019**, *58*, 9640–9645. [CrossRef] [PubMed]

32. Li, X.; Su, Z.; Zhao, Z.; Cai, Q.; Li, Y.; Zhao, J. Single Ir atom anchored in pyrrolic-N_4 doped graphene as a promising bifunctional electrocatalyst for the ORR/OER: A computational study. *J. Colloid Interface Sci.* **2022**, *607*, 1005–1013. [CrossRef] [PubMed]
33. Han, L.; Cheng, H.; Liu, W.; Li, H.; Ou, P.; Lin, R.; Wang, H.-T.; Pao, C.-W.; Head, A.R.; Wang, C.-H.; et al. A single-atom library for guided monometallic and concentration-complex multimetallic designs. *Nat. Mater.* **2022**, *21*, 681–688. [CrossRef] [PubMed]
34. Lv, X.; Wei, W.; Huang, B.; Dai, Y.; Frauenheim, T. High-Throughput Screening of Synergistic Transition Metal Dual-Atom Catalysts for Efficient Nitrogen Fixation. *Nano Lett.* **2021**, *21*, 1871–1878. [CrossRef]
35. Cao, N.; Zhang, N.; Wang, K.; Yan, K.; Xie, P. High-throughput screening of B/N-doped graphene supported single-atom catalysts for nitrogen reduction reaction. *Chem. Synth.* **2023**, 3. [CrossRef]
36. Janthon, P.; Kozlov, S.M.; Viñes, F.; Limtrakul, J.; Illas, F. Establishing the Accuracy of Broadly Used Density Functionals in Describing Bulk Properties of Transition Metals. *J. Chem. Theory Comput.* **2013**, *9*, 1631–1640. [CrossRef]
37. Rossmeisl, J.; Qu, Z.W.; Zhu, H.; Kroes, G.J.; Nørskov, J.K. Electrolysis of water on oxide surfaces. *J. Electroanal. Chem.* **2007**, *607*, 83–89. [CrossRef]
38. Tripković, V.; Cerri, I.; Bligaard, T.; Rossmeisl, J. The Influence of Particle Shape and Size on the Activity of Platinum Nanoparticles for Oxygen Reduction Reaction: A Density Functional Theory Study. *Catal. Lett.* **2014**, *144*, 380–388. [CrossRef]
39. Bajdich, M.; García-Mota, M.; Vojvodic, A.; Nørskov, J.K.; Bell, A.T. Theoretical Investigation of the Activity of Cobalt Oxides for the Electrochemical Oxidation of Water. *J. Am. Chem. Soc.* **2013**, *135*, 13521–13530. [CrossRef]
40. Valdés, Á.; Qu, Z.W.; Kroes, G.J.; Rossmeisl, J.; Nørskov, J.K. Oxidation and Photo-Oxidation of Water on TiO_2 Surface. *J. Phys. Chem. C* **2008**, *112*, 9872–9879. [CrossRef]
41. Ren, Y.; Tang, Y.; Zhang, L.; Liu, X.; Li, L.; Miao, S.; Sheng, S.; Wang, A.; Li, J.; Zhang, T. Unraveling the coordination structure-performance relationship in Pt_1/Fe_2O_3 single-atom catalyst. *Nat. Commun.* **2019**, *10*, 4500. [CrossRef] [PubMed]
42. Liu, J.; Xiao, J.; Luo, B.; Tian, E.; Waterhouse, G.I.N. Central metal and ligand effects on oxygen electrocatalysis over 3d transition metal single-atom catalysts: A theoretical investigation. *Chem. Eng. J.* **2022**, *427*, 132038. [CrossRef]
43. Medford, A.J.; Vojvodic, A.; Hummelshøj, J.S.; Voss, J.; Abild-Pedersen, F.; Studt, F.; Bligaard, T.; Nilsson, A.; Nørskov, J.K. From the Sabatier principle to a predictive theory of transition-metal heterogeneous catalysis. *J. Catal.* **2015**, *328*, 36–42. [CrossRef]
44. Deringer, V.L.; Tchougréeff, A.L.; Dronskowski, R. Crystal orbital Hamilton population (COHP) analysis as projected from plane-wave basis sets. *J. Phys. Chem. A* **2011**, *115*, 5461–5466. [CrossRef] [PubMed]
45. Yan, T.; Li, X.; Wang, Z.; Cai, Q.; Zhao, J. Interface engineering of transition metal-nitrogen-carbon by graphdiyne for boosting the oxygen reduction/evolution reactions: A computational study. *J. Colloid Interface Sci.* **2023**, *649*, 1–9. [CrossRef]
46. Wang, E.; Zhang, B.; Zhou, J.; Sun, Z. High catalytic activity of MBenes-supported single atom catalysts for oxygen reduction and oxygen evolution reaction. *Appl. Surf. Sci.* **2022**, *604*, 154522. [CrossRef]
47. Yang, C.; Wu, Y.; Wang, Y.; Zhang, H.-N.; Zhu, L.-H.; Wang, X.-C. Electronic properties of double-atom catalysts for electrocatalytic oxygen evolution reaction in alkaline solution: A DFT study. *Nanoscale* **2022**, *14*, 187–195. [CrossRef]
48. Ling, C.; Shi, L.; Ouyang, Y.; Zeng, X.C.; Wang, J. Nanosheet Supported Single-Metal Atom Bifunctional Catalyst for Overall Water Splitting. *Nano Lett.* **2017**, *17*, 5133–5139. [CrossRef]
49. Fu, Z.; Ling, C.; Wang, J. A $Ti_3C_2O_2$ supported single atom, trifunctional catalyst for electrochemical reactions. *J. Mater. Chem. A* **2020**, *8*, 7801–7807. [CrossRef]
50. Liu, F.; Song, L.; Liu, Y.; Zheng, F.; Wang, L.; Palotás, K.; Lin, H.; Li, Y. Using the N≡N dipole as a theoretical indicator for estimating the electrocatalytic performance of active sites in the nitrogen reduction reaction: Single transition metal atoms embedded in two dimensional phthalocyanine. *J. Mater. Chem. A* **2020**, *8*, 3598–3605. [CrossRef]
51. Zhang, Q.; Asthagiri, A. Solvation Effects on DFT Predictions of ORR Activity on Metal Surfaces. *Catal. Today* **2019**, *323*, 35–43. Available online: https://www.sciencedirect.com/science/article/pii/S0920586118310885 (accessed on 7 September 2018). [CrossRef]
52. Peng, Y.; Hajiyani, H.; Pentcheva, R. Influence of Fe and Ni Doping on the OER Performance at the Co_3O_4(001) Surface: Insights from DFT+U Calculations. *ACS Catal.* **2021**, *11*, 5601–5613. [CrossRef]
53. Kresse, G.; Furthmüller, J. Efficient iterative schemes for ab initio total-energy calculations using a plane-wave basis set. *Phys. Rev. B* **1996**, *54*, 11169–11186. [CrossRef]
54. Kresse, G.; Hafner, J.J.P.R.B. Ab initio molecular dynamics for open-shell transition metals. *Phys. Rev. B* **1993**, *48*, 13115–13118. [CrossRef]
55. Kresse, G.; Furthmüller, J. Efficiency of ab-initio total energy calculations for metals and semiconductors using a plane-wave basis set. *Comput. Mater. Sci.* **1996**, *6*, 15–50. [CrossRef]
56. Perdew, J.P.; Burke, K.; Ernzerhof, M. Generalized Gradient Approximation Made Simple. *Phys. Rev. Lett.* **1996**, *77*, 3865–3868. [CrossRef]
57. Perdew, J.P.; Burke, K.; Wang, Y. Generalized gradient approximation for the exchange-correlation hole of a many-electron system. *Phys. Rev. B* **1996**, *54*, 16533–16539. [CrossRef]
58. Perdew, J.P.; Chevary, J.A.; Vosko, S.H.; Jackson, K.A.; Pederson, M.R.; Singh, D.J.; Fiolhais, C. Atoms, molecules, solids, and surfaces: Applications of the generalized gradient approximation for exchange and correlation. *Phys. Rev. B* **1992**, *46*, 6671–6687. [CrossRef]
59. Perdew, J.P.; Wang, Y. Accurate and simple analytic representation of the electron-gas correlation energy. *Phys. Rev. B* **1992**, *45*, 13244–13249. [CrossRef]

60. Blöchl, P.E. Projector augmented-wave method. *Phys. Rev. B* **1994**, *50*, 17953–17979. [CrossRef]
61. Grimme, S.; Ehrlich, S.; Goerigk, L. Effect of the damping function in dispersion corrected density functional theory. *J. Comput. Chem.* **2011**, *32*, 1456–1465. [CrossRef]
62. Mathew, K.; Sundararaman, R.; Letchworth-Weaver, K.; Arias, T.A.; Hennig, R.G. Implicit solvation model for density-functional study of nanocrystal surfaces and reaction pathways. *J. Chem. Phys.* **2014**, *140*, 084106. [CrossRef]
63. Nørskov, J.K.; Rossmeisl, J.; Logadottir, A.; Lindqvist, L.; Kitchin, J.R.; Bligaard, T.; Jónsson, H. Origin of the Overpotential for Oxygen Reduction at a Fuel-Cell Cathode. *J. Phys. Chem. B* **2004**, *108*, 17886–17892. [CrossRef]
64. Man, I.C.; Su, H.-Y.; Calle-Vallejo, F.; Hansen, H.A.; Martínez, J.I.; Inoglu, N.G.; Kitchin, J.; Jaramillo, T.F.; Nørskov, J.K.; Rossmeisl, J. Universality in Oxygen Evolution Electrocatalysis on Oxide Surfaces. *ChemCatChem* **2011**, *3*, 1159–1165. [CrossRef]